Supplementary Materials

I. SAMPLE CONSTRUCTION

Two sets of commercial porous polycarbonate films (barriers) were purchased from Sterlitech Corporation (Kent, WA). The films had a thickness of approximately 6 μm, and pore density of approximately 8 pores/μm^2 as revealed via Atomic Force Microscopy shown in Fig. 1b.

Short-range disorder (A, B)—The polycarbonate films were cut in rectangular pieces of 0.95 mm in width and 7 mm in length with a scalpel and stacked in a layered geometry along the x axis (Fig. 1c-Fig. S1c) by hand using tweezers. The films were then placed in a rectangular NMR glass tube purchased from F&D Glass (Millville, NJ) (1 mm in height, 1 mm in width, 9 mm in length), filled with water and sonicated for 3 minutes. The samples were inspected under a microscope to avoid bubbles which may distort the RF and gradient fields. Two SR samples were constructed: one using the films with 15 nm pore diameter (A in Fig. 1c) and one using the films with 45 nm pore diameter (B in Fig. 1c). SR samples had 86–87 films stacked along x resulting in a predicted $\bar{a} \simeq 12$ μm. The white lines in Fig.1a of the main text represent the gaps between the barriers and the dark gray lines represent the barriers; the black line on the top right of the image is the edge of the NMR glass tube. This mean distance is maintained by compressing the stacked barriers before placing them in the NMR tube. The probability distribution of barrier placement of samples A and B is shown in Fig. S7 and points towards a non-Poisonian distribution. In addition, sample A revealed a large patch of large gaps in the barrier placement which may originate from the nature of sample construction.

Hyperuniform disorder (C)—The same set of 45 nm pore diameter polycarbonate permeable films was used to create the sample exhibiting hyperuniform disorder (sample C in Fig. 1c). In addition to the films, a customized set of spacers was used to achieve a semi-periodic geometry. Fig. S1a-b shows a cartoon representation of the sample exhibiting hyperuniform disorder (HU). The permeable membranes are shown in red. The yellow parts act as spacers between the barriers to control the geometry. An optical microscopy image is shown in Fig. S1d. The black regions represent the copper plates and the gray lines are the barriers between them. The white region on the bottom left shows the edge of the NMR glass tube. The thickness of the plates was $\sim (45 \pm 4)$ μm. The spacers were designed in the lab using Google Sketchup and built by Micron Solutions LLC (Salt Lake City, UT); the spacers had a length of 7 mm, 0.95 mm width, and a thickness of 45 μm. The thickness of the films was chosen so that the experimental errors in the placement of the films act as random drifts resulting in hyperuniformity (see main text) [1]. The spacers were made of copper and designed with an open end to minimize eddy currents. The resulting sample was made by placing the films and spacers in an alternating fashion.

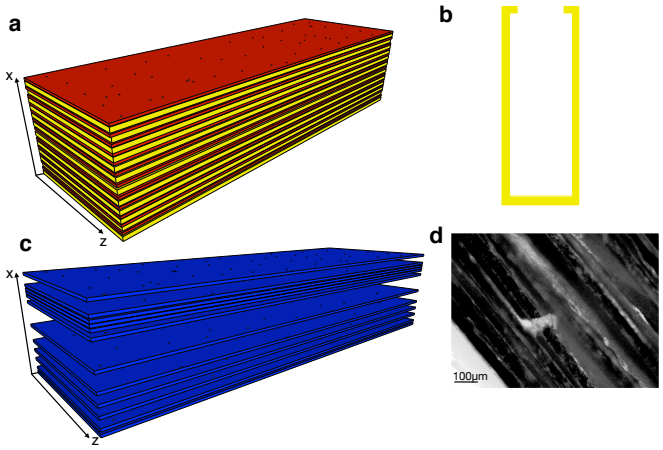

FIG. S1. **Sample exhibiting hyperuniform and short-range disorder** a) Cartoon representation of the sample. The red sheets represent the permeable barriers and the yellow parts act as a separation to achieve the hyperuniformity. b) Cartoon representation of the copper plates that were inserted in the sample in order to create the layered geometry. c) Cartoon representation of one of the SR samples. d) Representative optical microscopy image of the HU sample. Rectangular copper plates were inserted to achieve hyperuniformity.

II. COMPUTATION OF $\Gamma(k)$

The behavior of the density correlation function $\Gamma(k)$ at low k values may reveal the qualitative differences between samples not visible to the naked eye (Fig. 1d of main manuscript). However lack of averaging over disorder realizations result in noisy $\Gamma(k)$. In addition, the lack of long length scales apparent in the present experimental data do not allow for adequately observe the low-k scaling of $\Gamma(k)$. Fig. S8 shows simulated data of three different realizations of disorder of length L shown in black in Fig.S8a. The single averaging shown in red in Fig. S8 is performed by computing $\Gamma(k)$ for each line and subsequent averaging. This would yield a $\Gamma(k)$ with low k values of the order of $1/L$ (where L is the length of each sample). Note that averaging over disorder realizations reduces the noise. This method results in a less noisy $\Gamma(k)$ but with lacks a clean low-k scaling. The second method includes concatenating the three one dimensional lines and computing $\Gamma(k)$ (shown in green in Fig.S8). This would yield a $\Gamma(k)$ with low k values of the order of $1/3L$ but noise is apparent due to the lack of averaging. The last method includes concatenating the three lines N times in a random order, computing $\Gamma(k)$ and taking the average as shown in Fig. S8a in blue. This method results in $\Gamma(k)$ with low k values of the order of $1/3L$ with considerably less noise compared to green (where there is no averaging).

The third method was chosen for the computation of $\Gamma(k)$ presented in the main manuscript. The samples where digitized resulting in approximately 1000 one dimensional lines

of length L similar to the black samples in simulation. The 1d lines where then randomly concatenated 20 times and the resulting $\Gamma(k)$ where averaged.

III. DIFFUSION NMR

All experiments were performed on a 4.2 Tesla Tecmag Apollo system using a homemade probe equipped with high magnetic field gradients [2, 3]. The gradient coil was composed of two Maxwell pairs of 44 and 6 loops and had a diameter of 8 mm. The gradient set was capable of delivering magnetic field gradients of approximately 90 G/cm/Amp along the "z" direction (of the main magnetic field). Gradient was aligned in the direction normal to the surface of the permeable barriers (shown as x in the main text for the sake of more general notation). The temperature was set to 25°C and was regulated to within 0.5°C; at this temperature the theoretical diffusion coefficient is $D_0 = 2.30\ \mu\mathrm{m}^2/\mathrm{ms}$ [4]. Sample heating due to the application of high magnetic field gradients was tested based on chemical shift temperature measurements in methanol [5]; temperature variations were found to be less than 2% (°C).

The applied magnetic field gradients g_m ranged from approximately 5 G/cm to 1,000 G/cm and were calibrated using the theoretical diffusion coefficient at 25°C. Two pulse sequences were used for measuring the diffusion coefficient. For diffusion times, t, between 1 ms to 50 ms the pulse sequence is shown in Fig. S2a [6]. For t between 50 ms – 4.5 s the sequence is shown in Fig. S2b [7, 8]. For the diffusion measurements, the number of averages ranged from 160-700 resulting in total time of approximately 2 weeks for acquiring a single $D(t)$ curve (i.e. for one sample). Note that the between experiments (single data point of the $D(t)$ curve) the NMR magnet was spot checked for drifts which would alter the resonance frequency.

There are four basic causes that artificially alter the measured diffusion coefficient: eddy currents, magnetic field inhomogeneities, surface relaxation, and higher order terms in the cumulant expansion [9]. Sinusoidal pulses were used to mitigate ring-down effects which may result in slight errors in the q-space trajectory [10]. In addition, π pulses were used to refocus evolution under the background field gradients at time 4τ. The pulse sequences were tested on unrestricted water (Fig. 2a of main text), and no time-dependence was observed, as expected, which provided further evidence that these instrumental effects are small and do not alter the measured diffusion coefficient. The surface relaxation was also found to be minimal due to the relatively long spin-lattice relaxation times of H_2O imbedded in the polycarbonate films ($T_1 \simeq 1.8$ s). Lastly, higher order cumulants were suppressed by keeping the product $bD_0 < 1$ so that $\ln S \simeq -bD_0$ for all diffusion times probed in this work. The diffusion weighting parameter $b \sim (g_m\delta)^2 t$ was fixed to $b = 0.40\ \mathrm{ms}/\mu\mathrm{m}^2$.

Fig. S2 highlights the pulse sequences used in this work. The time interval Ξ was varied for each experiment from approximately 50 μs to 4.5 s. The gradient pulse width was $\delta = 120\ \mu$s for diffusion times of 1 ms to 1.3 ms and $\delta = 240\ \mu$s for diffusion times of 1.4 ms to 4.5 s. The $\pi/2$ pulse had a duration of $pw = 5\ \mu$s and the π a duration of 10 μs. The delay τ was 50 μs for the pulse sequence for short times and 500 μs for the pulse sequence for long times. The crushing gradient δ_c had a duration of 150 μs and is used to spatially dephase any single quantum coherence left after the $\pi/2$ pulse. The time interval T between the $\pi/2$ pulses was 2 ms and is used to push the echo further in time to mitigate ring down effects. The total diffusion time reported in Fig. 2 and Fig. 3 includes the time intervals that the molecules acquire the phase $e^{i\phi}$ (from the first gradient pulse until the last gradient pulse) due to the gradients and is given by $t = \delta + \tau + 2pw + \tau + \delta + \Xi + \delta + \tau + 2pw + \tau + \delta$. Or equivalently,

$$t = 4(\delta + \tau + pw) + \Xi. \tag{1}$$

The short-time regime

The pulse sequence used for diffusion times between 1 to 50 ms is shown in Fig. S2a [6]. The use of bipolar gradients compensate for the eddy currents induced by the fast changing current. It should be noted here that the background gradient g_0 was estimated based on the measured line width, $f = 350$ Hz, and sample size of $L \simeq 1$ mm, and found to be $g_0 \simeq 0.8$ G/cm. Therefore the background gradients are not expected to introduce any artificial fluctuations in the measured diffusion coefficient at short times.

The shaped gradient pulses alternate the form of b given in ref. [6]. The spatial wavenumber is given by $q(t) = \gamma \int_0^t dt' g(t')$ where $g(t)$ is the gradient waveform with respect to time. The attenuation of magnetization due to the the gradients is given by $-D_0 \int_0^t dt' q^2(t')$. [9, 10] For the pulse sequence shown in Fig. S2a the signal attenuation is given by,

$$S(g_m) = -D_0\Big(16g_m^2\tau\gamma^2\delta^2 + 22g_m^2\gamma^2\delta^3 + 16g_m^2\gamma^2\delta^2\Xi\Big)\frac{1}{\pi^2}. \tag{2}$$

In eq. (2), g_m is the maximum gradient strength and γ is the ^{1}H gyromagnetic ratio. Note that the term proportional to Ξ will dominate for $\Xi > 8$ ms. The phase cycling used for the short-time measurements is provided in ref. [6].

The long-time regime

The pulse sequence used for diffusion times between 50 ms to 4.5 s is shown in Fig. S2b [7, 8]. For the long time measurements, applying a fixed b-value requires reducing the applied gradient g_m, such that it may become comparable with susceptibility-induced background gradients g_0 which may alter the q-space trajectory. Asymmetric pulses were used to mitigate the cross-term proportional to $g_0 g_m$ in the cumulant expansion during both encoding and decoding periods. Due to the sinusoidal shaped gradient pulses, we recalculated the

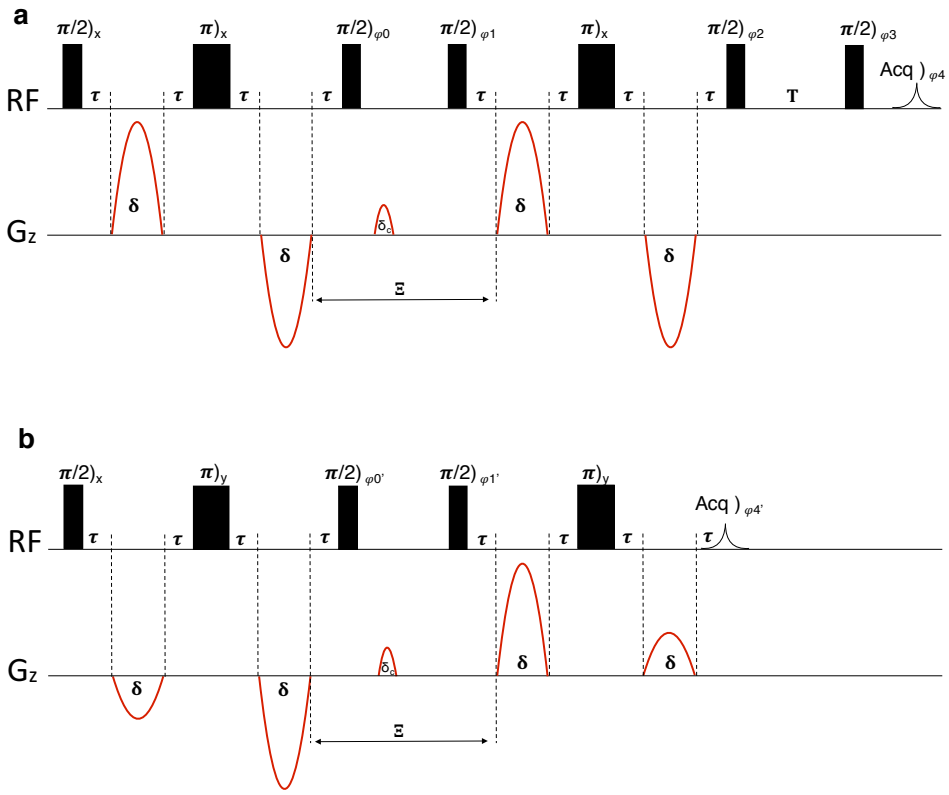

FIG. S2. **NMR pulse sequences used in this work.** Shaped pulses were used to mitigate ringdown effects which introduce imperfections in the gradient pulses and result in errors in the k-space trajectories [10]. In addition, the π pulses refocus evolution under the background gradients colinear with the Zeeman field at time 4τ. a) NMR pulse sequence used for measuring diffusion for times between 1 to 50 ms. [6] The use of bipolar magnetic field gradient pulses compensate for eddy currents. The phases of the RF pulses for this pulse sequence are given in ref. [6]. b) NMR pulse sequence used for measuring diffusion for times between 50 ms to 4.5 s. [7, 8] The use of assymetric magnetic field gradient pulses cancels the cross term between the applied magnetic field gradient g and the background gradient, g_b, after decoding. The phases of the RF pulses for this pulse sequence are given in ref. [7].

expression for the b-value as compared to refs. [7, 8]. The signal attenuation for the pulse sequence shown in S2b is given by,

$$S(g_m) = -D_0\Big((g_0^2 + g_0'^2)\big[\frac{2\tau^3\gamma^2}{3} + 2\tau^2\gamma^2\delta + 2\tau\gamma^2\delta^2 + \frac{2\gamma^2\delta^3}{3}\big] + \big[-2g_{m2}\gamma\delta - 2g_{m2}\gamma\delta\eta\big]^2\frac{\Xi}{\pi^2} + \big[3\gamma^2\delta^3 + 8\gamma^2\delta^3\eta + 16\tau\gamma^2\eta^2 + 11\gamma^2\delta^3\eta^2\big]\frac{g_{2m}^2}{\pi^2}\Big), \quad (3)$$

with,

$$\eta = -\frac{\delta^2(-4+\pi^2)}{\pi^2(4\tau^2 + 8\tau\delta + \frac{4\delta^2}{\pi^2} + 3\delta^2)}. \quad (4)$$

In the above equation g_0 and g_0' are the values of the background gradients during the encoding and decoding time intervals and were estimated to be approximately 0.8-1 G/cm based on the linewidth. The ratio $\eta = g_{m2}/g_{m1}$ is defined by eq. (4); choosing an appropriate η suppresses the $g_0 g_m$ term in the signal attenuation. Note that the term proportional to Ξ dominates for $\Xi > 20$ ms. The phase cycling for long-time measurements is provided in ref. [7].

IV. NUMERICAL DIFFERENTIATION

The computation of $D_{\rm inst}$ reported in Fig. 2b requires taking the derivative of the measured cumulative diffusion coefficient as $D_{\rm inst}(t) = \partial_t[tD(t)]$. This operation amplifies experimental noise and therefore a Savitzky-Golay (SG) filter with a dynamical window that increases with respect to time was implemented [11]. The minimum SG window size and polynomial order were chosen such that $\chi^2/{\rm dof}$ and error ϵ_ϑ in ϑ is minimal. We chose a filter with polynomial order 2, and a filtering window of $\pm 60\%$ of the central time point on the fitting polynomial. A least squares fit with ${\rm dof} = 2$

was used for ϑ and c by fixing the D_∞ value to that from the $D(t)$ fit at long t. The resulting $\chi^2/\mathrm{dof} \approx 2$ for the HU and $\chi^2/\mathrm{dof} \approx 3$ for the SR sample B. For the SR sample A, the χ^2/dof had a higher value ($\simeq 7$) due to the increased fluctuations in the experimental data. Statistical analysis of the least squares fit results of the SG window size with respect to ϑ and ϵ_ϑ is shown in the Supplementary Fig. S4. The χ^2/dof with respect to SG window and the least squares fit results with respect to the initial conditions are also shown in Supplementary Fig. S4-S5.

V. DIFFUSIVE PERMEABILITY OF A SINGLE BARRIER

Combining the results of Fig. 2 and 3 of the main text, we can go one step further and quantify the permeability of the barriers used to construct the samples.

Parameter $\zeta = \frac{SD_0}{2V\kappa d}$, introduced in ref. [12], is a dimensionless "barrier strength" that depends on the permeability and density of the barriers, and quantifies the ability of barriers to slow down the diffusion. The universal limit of the diffusion coefficient D_∞, is then directly connected [12] to ζ, as $D_\infty \simeq D_0/(1+\zeta)$. For the case of $d = 1$, which is the case in our work, the above equation is exact, and therefore determining the surface-to-volume ratio, $S/V \equiv 2/\bar{a}$ and D_∞ allows for computing the diffusive permeability κ of a single barrier. The average distance between the barriers was determined from the optical microscopy images shown in Fig. 1 of the main text (cf. Table I for values of $\bar{a}$). The universal limit D_∞ was determined from the long-time regime by performing least squares fit with $\mathrm{dof} = 3$ to $D(t)$ (raw data shown in Fig. S3).

For the SR sample created with barriers having an average pore diameter of 15 nm (sample A in Fig. 1 of the main text), $D_\infty|_{15\mathrm{nm}} = 0.42 \pm 0.04\ \mu\mathrm{m}^2/\mathrm{ms}$, $\zeta|_{15\mathrm{nm}} \simeq 4.6$ resulting in $\kappa|_{15\mathrm{nm}} = 0.04 \pm 0.01\ \mu\mathrm{m/ms}$. For the SR sample created with barriers having an average pore diameter of 45 nm (sample B in Fig. 1 of the main text), $D_\infty|_{45\mathrm{nm}} = 0.58 \pm 0.05\ \mu\mathrm{m}^2/\mathrm{ms}$, $\zeta|_{45\mathrm{nm}} \simeq 2.7$ resulting in $\kappa|_{45\mathrm{nm}} = 0.06 \pm 0.02\ \mu\mathrm{m/ms}$. Note that for the sample exhibiting hyperuniform disorder, the spacers used for controlling the geometry will artificially lower D_∞ resulting a lower diffusive permeability κ. It is therefore more accurate to determine the permeability of the barriers using the diffusion coefficient from the samples exhibiting short-range disorder. Note that the fact that the bulk material of the films is conductive will alter measured permeability as it "short-cuts" the conduction through the pores. A detailed study of the material geometry and permeability is beyond the scope of this work.

VI. STATISTICS OF LEAST SQUARES FIT

Cumulative diffusion coefficient D

A least squares power law fitting procedure with three degrees of freedom was used to estimate the dynamical exponent $\tilde{\vartheta}$, the universal diffusion coefficient at long times D_∞, and the coefficient c according to,

$$D(t) = D_\infty + ct^{-\tilde{\vartheta}}. \tag{5}$$

The results are shown as solid lines in Fig. S3 and the χ^2/dof for all three fitting procedures was approximately 0.8. The resulting $\tilde{\vartheta}$ from the least squares fitting procedure is shown in Table I of the main text.

Instantaneus diffusion coefficient D_{inst}

Figure S4 shows the statistics of SG window size and polynomial order for the χ^2/dof and $\vartheta \pm \epsilon_\vartheta$ for the sample exhibiting hyperuniform disorder. The statistics for different SG window size (as percentage) are shown in Fig. S5a. A two degrees of freedom least squares fit was used for ϑ and c by using the D_∞ value from the cumulative diffusion coefficient fit. A least squares fit window was chosen such that the χ^2/dof was minimum. The resulting ϑ was observed to converge to the expected theoretical values as the SG window is increased. The computed χ^2/dof is shown to decrease with respect to the SG window and plateaus to a reasonable value ($\simeq 3$) for short-range disorder (Sample B), and hyperuniform disorder ($\simeq 2$) (Sample C). On the other hand, for the other sample exhibiting short-range disorder (Sample A) the χ^2/dof had a higher value ($\simeq 7$) due to increased fluctuations in the experimental data. The results of the least squares fit procedure for ϑ with respect to the initial conditions are shown in Fig. S5b-c-d and show a reasonable Gaussian shape with a tail for the samples A-B (green-blue) and a bimodal distribution for C (red).

Surface-to-volume ratio S/V

Fig. S6 highlights statistics of one and two degrees of freedom least squares fit results ($\bar{a}$ and D_0), with respect to the dimensionless ratio t/τ_D. Each point in Fig. S6 represents the first point of a least squares fit with a time range varying from $0.05\tau_D$ for $t \ll \tau_D$ to $\tau_D/2$ for $t \simeq \tau_D$. Note that the increments of time δt where always much smaller than the window of the fit. Therefore the results of Fig. S6 correspond to local slopes along $D(t)$ in Fig. 3. Fig. S6a-b shows the fit results of the mean barrier spacing $\bar{a}$ and free diffusion coefficient D_0 along with the known values (black lines). It is evident that the fit results agree with the predictions for $t/\tau_D < 0.1$ suggesting that the fitted S/V will be substantially underestimated if not at this time regime. Fig. S6c highlights the fitted $\bar{a}$ by fixing D_0 to the theoretical value at the corresponding temperature ($D_0 = 2.30\ \mu\mathrm{m}^2/\mathrm{ms}$ at 25°C).

[1] S. Torquato and F. H. Stillinger, "Local density fluctuations, hyperuniformity, and order metrics," Phys. Rev. E **68**, 041113 (2003).

[2] W. Zhang and D.G. Cory, "Pulsed gradient NMR probes for solid state studies," J. Magn. Reson. **132**, 144–149 (1998).

[3] B. H. Suits and D. E. Wilken, "Improving magnetic field gradient coils for nmr imaging," J. Phys E. Sci. Instrum. **22**, 565 (1989).

[4] M. Holz, S. R. Heil, and A. Sacco, "Temperature-dependent self-diffusion coefficients of water and six selected molecular liquids for calibration in accurate 1H NMR PFG measurements," Phys. Chem. Chem. Phys. **2**, 4740–4742 (2000).

[5] A. L. Van Geet, "Calibration of methanol nuclear magnetic resonance thermometer at low temperature," Anal. Chem.Chemistry **42**, 679–680 (1970).

[6] D. H. Wu, A. D. Chen, and C. S. Johnson, "An improved diffusion-ordered spectroscopy experiment incorporating bipolar-gradient pulses," J. Magn. Reson. Ser. A **115**, 260–264 (1995).

[7] P. Z. Sun, J. G. Seland, and D. Cory, "Background gradient suppression in pulsed gradient stimulated echo measurements," J. Magn. Reson. **161**, 168 – 173 (2003).

[8] P. Galvosas, F. Stallmach, and J. Kärger, "Background gradient suppression in stimulated echo NMR diffusion studies using magic pulsed field gradient ratios," J. Magn. Reson. **166**, 164 – 173 (2004).

[9] V. G. Kiselev, "The cumulant expansion: an overarching mathematical framework for understanding diffusion nmr," Diffusion MRI: Theory, Methods, and Applications , 152–168 (2011).

[10] A. Sodickson and D. G. Cory, "A generalized k-space formalism for treating the spatial aspects of a variety of NMR experiments," Prog. Nucl. Mag. Res. Sp. **33**, 77–108 (1998).

[11] A. Savitzky and M. J. E. Golay, "Smoothing and differentiation of data by simplified least squares procedures." Anal. Chem. **36**, 1627–1639 (1964).

[12] D. S. Novikov, E. Fieremans, J. H. Jensen, and J. A. Helpern, "Random walks with barriers," Nat. Phys. **7**, 508–514 (2011).

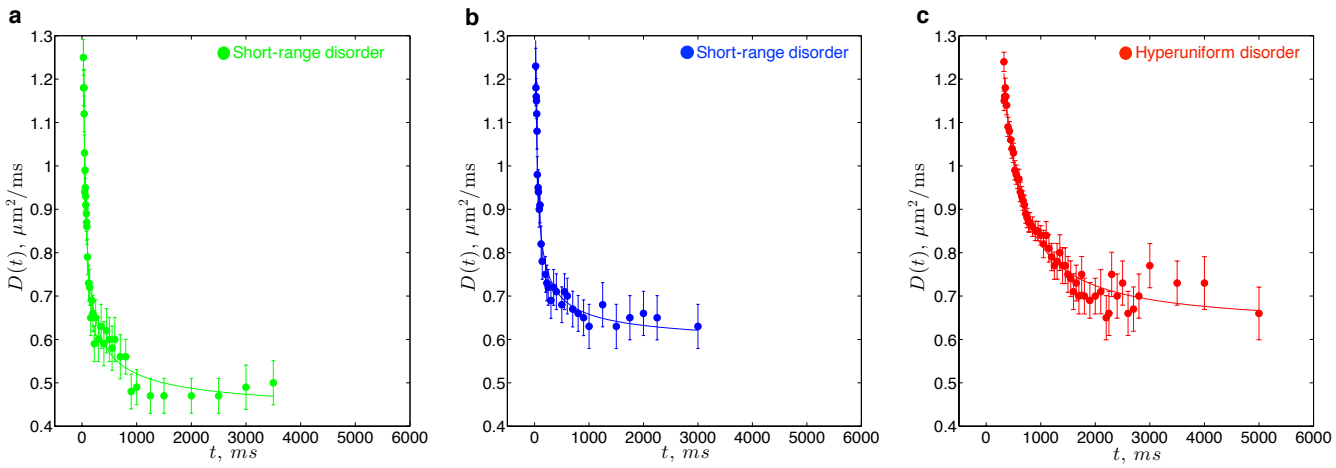

FIG. S3. **Measured diffusion coefficient with respect to the diffusion time for the three disordered samples used in this work.** The solid line corresponds to a least squares fit with three degrees of freedom to eq. (5). a) Time dependence of the diffusion coefficient for the SR sample A. b) Time dependence of the diffusion coefficient for the SR sample B. C) Time dependence of the diffusion coefficient for the HU sample C.

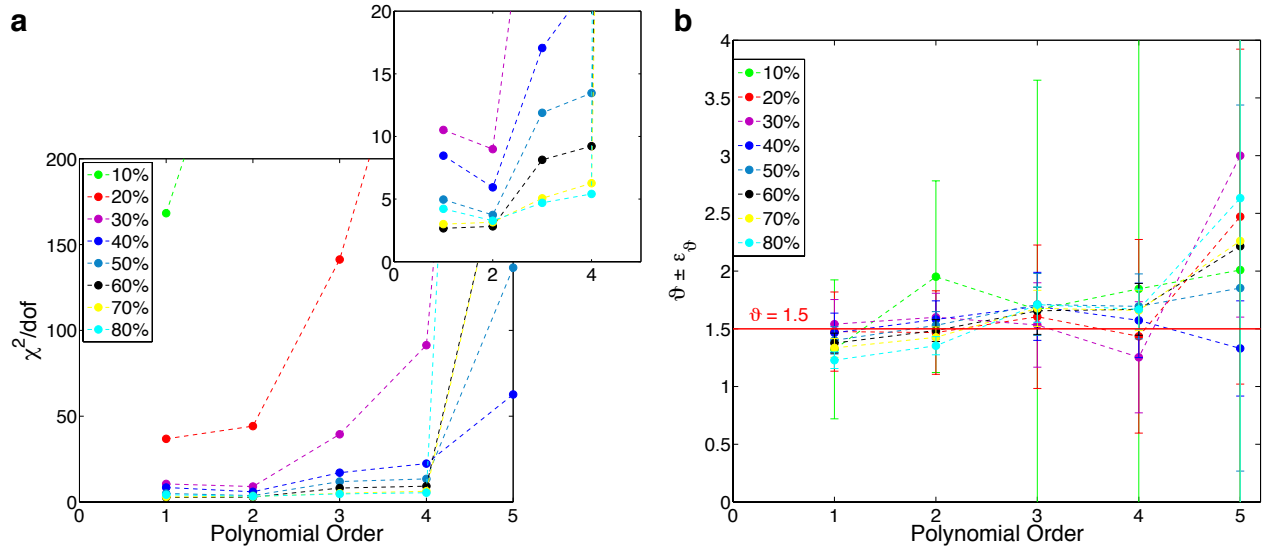

FIG. S4. **Statistics of the Savitzky-Golay smoothing procedure (percentage) with respect to the polynomial order for the sample exhibiting hyperuniform disorder (C-red).** a) χ^2/dof diverges as the polynomial order is increased. b) Least squares power law fit with two degrees of freedom reveals that the fitted value for ϑ converges to the expected power law for low polynomial order and converges for high polynomial order.

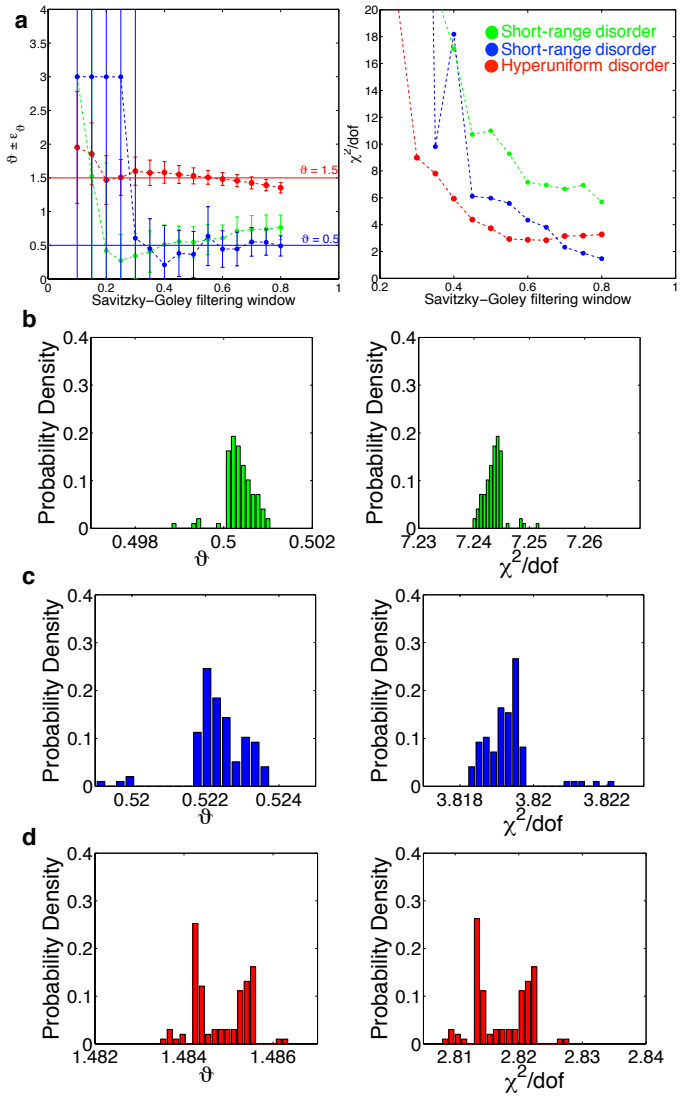

FIG. S5. **Statistics of the Savitzky-Golay smoothing procedure and least squares power law fit with two degrees of freedom.** a) Resulting power law least squares fit and error, $\vartheta \pm \epsilon_\vartheta$, with respect to Savitzky-Golay filtering window of the three disorder classes. As discussed in the text, increasing the filtering window reduces the noise, and thus the error, revealing the true exponent ϑ. Reduced χ^2 with respect to Savitzky-Golay filtering window of the three disorder classes. The chosen dynamic window for the three data sets was ± 0.6 (60%) of the central time point of the window. b-c-d) Statistics for the power law fit and reduced χ^2 of the filtered D_{inst} for the three disorder classes for multiple initial conditions. The resulting least squares fit parameters, ϑ and c (not shown) were robust for short-range disorder (blue) and hyperuniform disorder (red) as shown from the reduced χ^2 distribution. The resulting least squares fit parameters for short-range (green) don't show large deviation with respect to the initial conditions but the reduced χ^2 is high due to the increased scatter in the data.

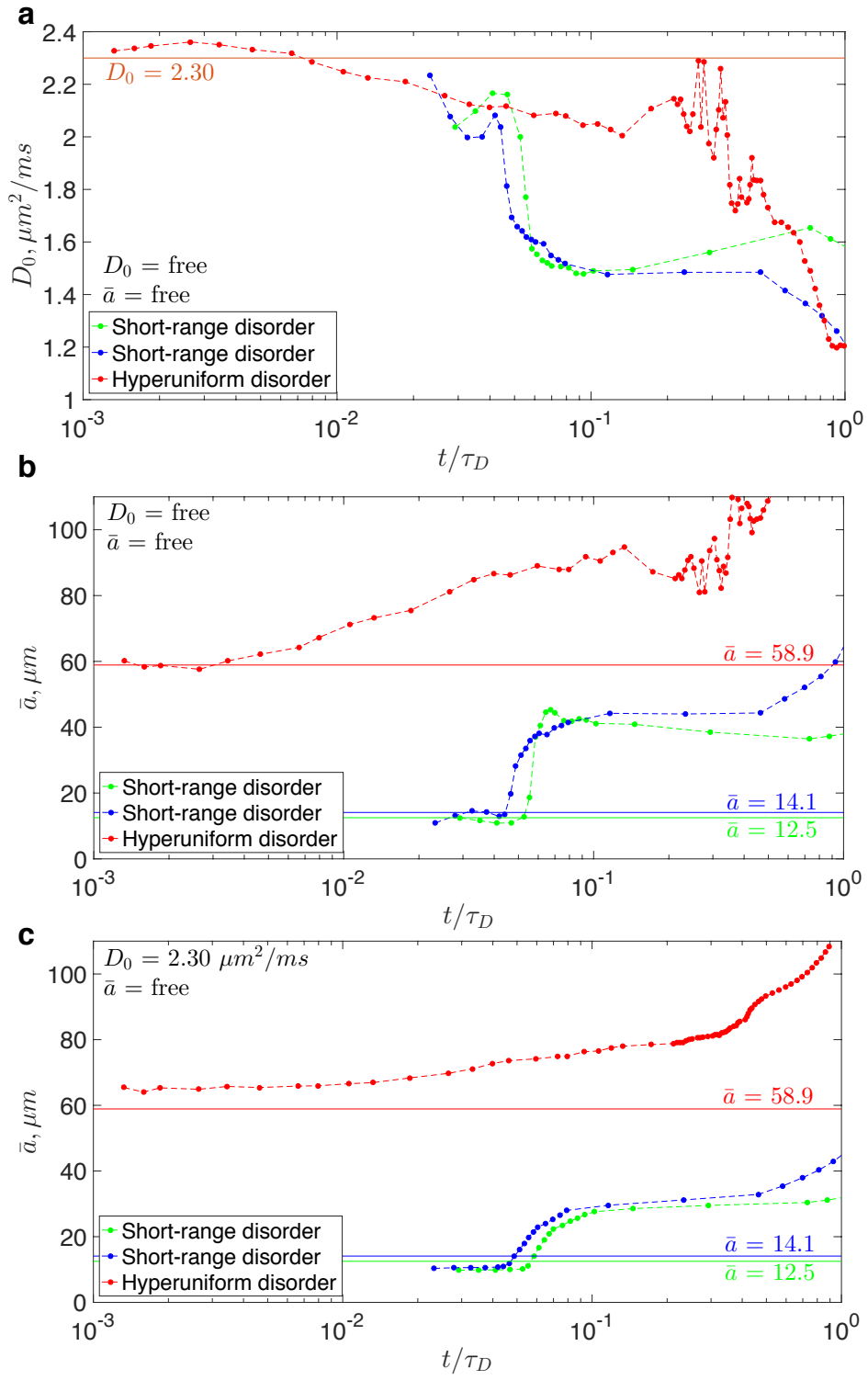

FIG. S6. **Statistics of the surface-to-volume ratio least squares fitting procedure with two (a-b) and one (c) degrees of freedom with respect to the fit window with a dynamic range.** Each point represents the first point of the fit. a) Fitted $\bar{a}$; b) D_0; c) $\bar{a}$ with respect to the fit window using a fixed $D_0 = 2.30\ \mu\text{m}^2/\text{ms}$.

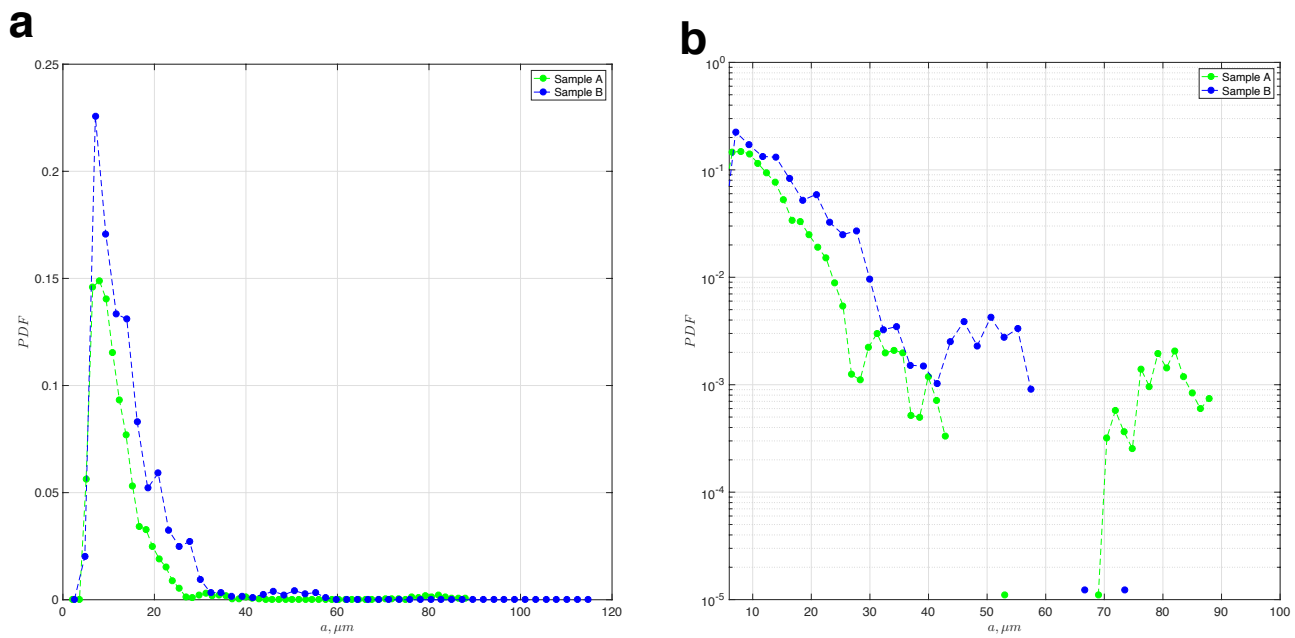

FIG. S7. **Probability density function, $P(a)$, of the barrier placement of the SR samples A and B.** a) $P(a)$ for the two SR samples. b) $P(a)$ shown in a semi-log plot points towards a Gaussian distribution and reveals no apparent large gaps between the barriers for Sample B. Sample A on the other hand revealed a patch of larger barrier placements around 80 μm.

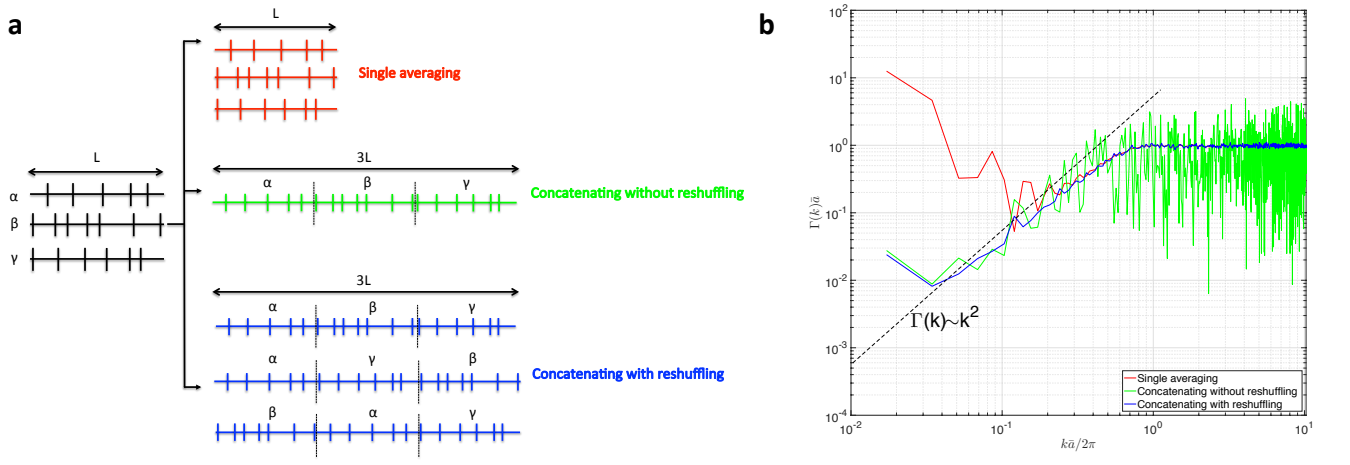

FIG. S8. **Description of alternative options for computing $\Gamma(k)$ of simulated HU disorder class.** a) Three ways of concatenating the data and perform the averaging. b) Resulting $\Gamma(k)$ for the three different options shown in (a).